Chapter 4

Synthesis and Characterisation of

$La_xSr_{2-x}MnO_4$

4.1 Introduction

Various dielectrics with positive permittivity have been extensively investigated in the past few decades. Polarization is the main response mechanism of materials with positive dielectric permittivity in electric field [221]. In recent years, materials with negative permittivity have attracted a great deal of attention due to their potential applications in electromagnetic shielding [119], capacitors [222], transistors [223], antennas [224], inductor design, and other electronic devices. As we know that, the responses of a certain material to electromagnetic waves are largely determined by two parameters: permittivity (ε) and permeability (μ). For conventional materials both permittivity and permeability are positive, the materials with negative permittivity or/and negative permeability display various disparate effects when exposed to electromagnetic waves. However, negative permittivity was firstly realized in metamaterials with an artificial structure of periodic metallic wires and rings [102,118,225], rather than from the point of view of materials, i.e., the intrinsic properties composition and microstructure. It is also worth important here to note that, negative permittivity is common in metals or a good kind of conductor. below their plasma frequency due to the plasmonic state of free electrons, but the plasma frequencies of metals are usually at ultraviolet band, which exceed much of the radio frequency [102,118,225]. If the same can be achieved at lower or even zero frequency, electrons would be attracted each other instead of repulsion, offering new opportunities in physics and electronics [117]. According to Drude model, the plasma frequency decreases with the decreasing carriers' density [226], of course the carriers in metals are free electrons. Hence radio frequency plasma oscillation can be achieved by some materials with suitable carrier concentration. On the basis of this, to realize optimum carrier concentration and thereby negative permittivity in radio frequencies, numerous works have been carried out in many polymer matrix composites [227–233], as well as many ceramic matrix composites [137,234], within these two classes the insulating polymers

or ceramics act as matrix and play an important role in diluting electrons concentration of metals or carbon materials. Thus, average electron concentration can be controlled by the contents of conductors to achieve a negative permittivity near the percolation threshold at certain frequency range [136,235]. Compared with metamaterials, composites take advantages on that the complicated artificial structures can be avoided but the designability of negative permittivity property can be still guaranteed. However, the anomalous dielectric behaviours in both metamaterials and composites are always based on the self-properties of building blocks or metallic fillers. In fact, negative permittivity property hinges on the concentration of carriers in materials [236]. From the perspective of relationships between negative permittivity and electrons, it's credible and significant to realize desirable negative dielectric performances in homogeneous materials of single phase.

The Sr_2MnO_4 is a two-dimensional perovskite like layer structure, in this structure it is easy to implant ions as dopants into the host lattice and hence manipulate its physical and chemical properties. The multivalency of Mn cation offers the opportunity to tune its oxidation state via optimum dopant and its concentration, which may change electrical properties further. Sr_2MnO_4 is isostructural to the K_2NiF_4, crystallized with a tetragonal unit cell in the space group I4/mmm [179]. The oxides of the K_2NiF_4-type belong to the n=1 member of the Ruddlesden–Popper (RP) phases of the general formula $A_{n+1}B_nO_{3n+1}$. The RP phases comprise n consecutive perovskite (ABO3) layers that alternate a rock-salt layer (AO) along the c-axis [179]. Doped and undoped Sr_2MnO_4 oxides have been reported as possible cathode materials for symmetrical solid oxide fuel cells (SOFCs) and solar cells [194,237]. By normal solid-state reaction method synthesis of Sr_2MnO_4 is a challenging task [165,238]. In the previous, I have discussed synthesis of single-phase Sr_2MnO_4 powder by quenching in the air from 1500°C to room temperature [238]. Further, partial replacement of Sr by La (concentration ≥ 0.25 mole %) can produce single phases via a normal solid-state ceramic route [48].

The physical properties like carrier concentration and electrical properties of Sr_2MnO_4 oxide can be changed by doping at the Sr/Mn site. As mentioned above, the negative permittivity property hinges on the carriers' concentration, a doner or acceptor type substitution in Sr_2MnO_4 may tune carrier concentration. And hence, in this chapter, we have tried to study the effect of La (doner) doping at the Sr site on electrical properties by synthesizing three compositions (with x=0.30, 0.50, 0.70) of the $La_xSr_{2-x}MnO_4$ system. To the best of our knowledge, no report is available in the literature on the temperature and frequency-dependent dielectric properties of La doped Sr_2MnO_4. In this chapter, the dielectric properties of La doped Sr_2MnO_4 were investigated by measuring real (Z') and imaginary (Z") components of the impedance, Z, in the temperature range 30-300 ^oC and in the frequency range 20 Hz - 2 MHz. The studied composition of La doped $La_xSr_{2-x}MnO_4$ system has showed negative dielectric behaviour at all measuring temperature and at all measuring frequencies.

4.2 Experimental

La substituted $La_xSr_{2-x}MnO_4$ (x = 0.3, 0.5 & 0.7) has been prepared using conventional solid-state reaction route. The starting compounds $SrCO_3$ (Sigma-Aldrich, purity ≥ 99.9%), MnO_2 (Sigma-Aldrich, purity ≥ 99%), and La_2O_3 (Alfa Aesar, purity ≥ 99.9%) were taken in the stoichiometric ratio and mixed in an Agate Mortar and Pestle by hand using acetone as mixing medium. The mixtures were then calcined for 24 hours at 1200 ^oC with intermediate grinding in a high-temperature furnace (HTRH-70/150, Carbolite Gero, UK). For microstructure, XPS, and electrical measurements, the pellets with a diameter 11-12 mm and a thickness of 2-3 mm were prepared using a hydraulic press by applying the pressure of 5 kN. Green pellets were sintered in a muffle furnace at 1500 ^oC for 12 hours and cooled to room temperature with normal cooling rate of 4 ^oC/min. For convenience, in succeeding sections

these samples have been addressed with a short name such as LSM3, LSM5, and LSM7 for $La_{0.3}Sr_{1.7}MnO_4$, $La_{0.5}Sr_{1.5}MnO_4$ and $La_{0.7}Sr_{1.3}MnO_4$, respectively.

The X-ray diffraction (XRD) pattern of the sintered pellets was recorded at room temperature using a diffractometer (Rigaku Miniflex II Desktop, Japan). The morphological fingerprints of fractured surfaces of the sintered pellets were recorded using a field emission Scanning Electron Microscope (Nova Nano SEM 450, USA). For dielectric/electrical properties measurements, circular surfaces of the sintered pellets were polished using emery paper of different grades and then coated with a thin and uniform layer of high-temperature silver paste. Real (Z') and imaginary (Z") parts of the impedance (Z) were measured as a function of the frequency (in the range of 20 Hz–2 MHz) and temperature (in the range of 30-300 ^oC), using an inductance-capacitance-resistance (LCR) meter (Agilent E-4980, USA). For studying the valence state of constituent element Mn present in bulk of the pellets, the pellets' surfaces were scorched and further polished with the various grades of emery paper. Thereafter, using an X-ray photoelectron spectrometer (Thermo Fisher Scientific K-Alpha, USA), operating at the high pressure of 5×10^{-11} Torr, the core spectra of Mn were recorded.

4.3 Results and Discussion

4.3.1 Crystal Structure

The X-ray diffraction (XRD) pattern of prepared compositions $La_xSr_{2-x}MnO_4$ (x = 0.3, 0.5 & 0.7) were recorded and shown in Fig. 4.1 (a). The XRD patterns were matched with the Crystallography Open Database (COD) for Sr_2MnO_4 (1008125). No distinct peaks corresponding to raw materials SrO, MnO_2, and La_2O_3 or expected secondary phase $Sr_7Mn_4O_{15}$ were observed in all samples, which confirmed the formation of single-phase solid solutions. A systematic shift of the peaks towards the higher angle side with increasing dopant (La) concentration (x) was observed. A magnified view of the shift of the peak corresponding to the

plane (103) and (110) is shown in the inset of the same figure. The ionic radius of La^{3+} is 1.21 Å, smaller than the ionic radius of Sr^{2+} (1.31 Å) in the same coordination number nine [239]. Therefore, the observed peak shift indicates the replacement of Sr^{2+} ions by La^{3+} ions in the Sr_2MnO_4 lattice.

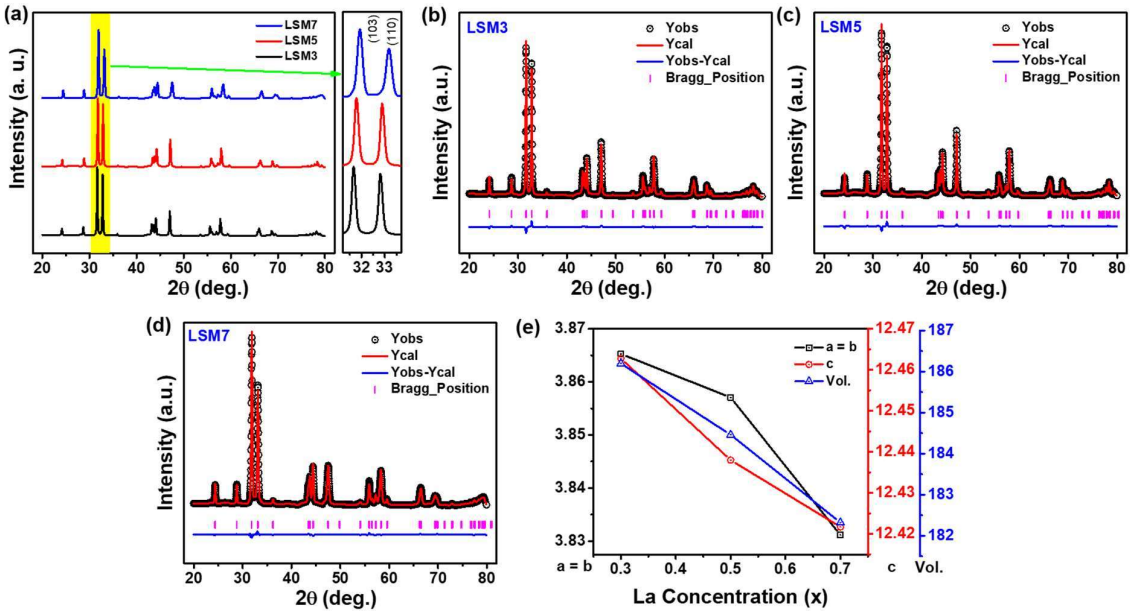

Figure 4.1. (a) Room temperature XRD pattern of the samples, (b, c, d, e) Rietveld refined XRD pattern of the samples (f) Variation of lattice parameters with La Concentration (x).

The structural parameters of the samples LSM3, LSM5 and LSM7 samples were obtained with the help of Rietveld refinement using the FullProf Suite software package. The structural refinement was carried out by considering the tetragonal structure and space group I4/mmm. The calculated XRD pattern obtained after the final refinement is shown in Fig. 4.1 (b, c, d). A good matching between the experimentally recorded and calculated XRD patterns was seen. The obtained structural parameters are summarized in Table 4.1. The value of these parameters for the sample SMQ (Sr_2MnO_4) is also shown in the Table 4.1 for comparison [238]. The variation of the lattice parameters and the unit cell volume with dopant (La) concentration (x) is shown in Fig. 4.1(e). The lattice parameters (a = b and c), as well as the unit cell volume, has increased with La doping at first for x = 0.3 composition, thereafter decreases on increasing

La concentration in the solid solution. The first increase in unit cell volume for x = 0.3 composition, and thereafter decrease in unit cell volume, with further increasing La concentration is consistent with the recorded XRD peak shift. The increase in Sr/La-O(1) and Mn-O(1) bond lengths for x = 0.3 composition in comparison with undoped Sr_2MnO_4, and further decrement in it with increasing La concentration (x) also confirms the same. The La doping at Sr cite(s) in Sr_2MnO_4 forces either reduction of Mn cation to Mn^{3+} oxidation state from Mn^{4+} state or incorporation of oxygen at inter-cite(s), O_i; due to its higher oxidation state (La^{3+}) in comparison with Sr^{2+}. According to defect chemistry the reduction Mn cation or incorporation of oxygen at inter-cite(s) in Kröger-Vink notations as follows:

$$La_2O_3 \rightarrow 2\left(La_{Sr^{2+}}^{3+}\right)^{\bullet} + 2O_o^{*} + \frac{1}{2}O_2(g) + 2e' \qquad (4.1)$$

$$(Mn_{Mn^{4+}}^{4+})^{\times} + e' = (Mn_{Mn^{4+}}^{3+})' \qquad (4.2)$$

Or,

$$\frac{1}{2}O_2(g) = O_i'' + 2h^{\bullet} \qquad (4.3)$$

The ionic radius of Mn^{3+} (0.64 Å) is greater than ionic radius of Mn^{4+} cation (0.53 Å) in six coordination number [239]. Therefore, the unit cell will expand due to this reduction. Similarly, the incorporation oxygen ion at inter-cite(s) will expand the unit cell volume. The expansion of unit cell volume will lead in the increment of lattice parameter as well as bond lengths. Here it is important to mention that, the ionic radius of La^{3+} (1.21 Å) is smaller than the ionic radius of Sr^{2+} cation (1.31 Å) in same coordination number nine [239]. As we know that the incorporation of smaller ionic radii element reduces the lattice parameters. Henceforth, the changes in lattice parameters, unit cell volume and bond lengths can be understood as. All have increased for x = 0.3 La concentration, in compare with undoped Sr_2MnO4, due to the

reduction of Mn cation(s) or incorporation of oxygen(s) at inter-cite(s) and thereafter all decreases with further increasing La concentration (above x = 0.3) due to the reduction produced by further incorporation of La (a smaller ionic radius element) in Sr_2MnO4 lattice.

To analyse the stability of prepared solid solutions, the value of the tolerance factor (t) and Global instability index (GII) has been calculated. In the case of layered perovskites, t estimates the compatibility of perovskite and rocksalt layer. While GII represents the instability of the structure and a larger GII indicates a less stable structure [240]. The equations for the calculation of the tolerance factor and Global instability index (GII) are given below:

$$t = \frac{\frac{(2-x)\times r_{Sr} + x \times r_{La}}{2} + r_O}{\sqrt{2} * (r_{Mn} + r_{Sn} + r_O)} \qquad (4.4)$$

where $r_{Sr}, r_{La}, r_{Mn}, r_O$ are the effective radii of Sr, La, Mn, O, respectively and x is the Sn concentration in the prepared samples. And,

$$GII = \frac{\sqrt{\sum_{i=1}^{N}\{\sum_j (S_{ij} - V_i)^2\}}}{N} \qquad (4.5)$$

where S_{ij} is the sum of the valence bonds around each ion and $V_i = \sum_j S_{ij}$. The value of S_{ij} is determined by the semi-empirical expression $S_{ij} = \exp[(R_o - R_{ij})/0.37]$, where R_o is a constant characteristic of the bond type. Calculated values of tolerance factor (t) and Global instability index (GII) are listed in table 4.1. Both tolerance factor (t) and the Global instability index (GII) have decreased with increasing La concentration (x). The Sr_2MnO_4 is stable only at temperatures higher than 1350 °C, below this temperature it decomposes in $Sr_7Mn_4O_{15}$ and SrO [165]. To stabilize Sr_2MnO_4 phase at lower temperatures approximately 30% of Mn ions should be present in Mn^{3+} state [73,241]. To achieve this goal, synthesis of Sr_2MnO_4 has been carried reducing atmospheres [241–244]. In previous chapter, the synthesis and stabilization of

undoped Sr_2MnO_4 at room temperature by quenching from high temperature (1500°C) to room temperature in the air is explained. The doping of La at Sr cites helps in stabilizing Sr_2MnO_4 phase at lower temperatures. Thus, La plays the same role as reducing atmospheres or quenching is playing in stabilizing Sr_2MnO_4 phase at lower temperatures. Here it is also important to mention that, the calculated values of t and GII of La substituted Sr_2MnO_4 are in the range of other reported A_2BO_4 compound [240,245,246].

Table 4.1. Structural parameters and reliability factors obtained by Rietveld refinement of the XRD patterns.

Sample Composition	Sr_2MnO_4	$La_{0.3}Sr_{1.7}MnO_4$	$La_{0.5}Sr_{1.5}MnO_4$	$La_{0.7}Sr_{1.3}MnO_4$
Sample Code	**SMQ**	**LSM3**	**LSM5**	**LSM7**
a = b (Å)	3.795	3.865	3.857	3.831
c (Å)	12.500	12.462	12.438	12.422
Cell Volume ($Å^3$)	180.636	186.198	184.459	182.322
Sr (4e)	(0, 0, 0.357)	(0, 0, 0.358)	(0, 0, 0.357)	(0, 0, 0.355)
Mn/Sn (2a)	(0, 0, 0)	(0, 0, 0)	(0, 0, 0)	(0, 0, 0)
O (1) (4c)	(0, 0.5, 0)	(0, 0.5, 0)	(0, 0.5, 0)	(0, 0.5, 0)
O (2) (4e)	(0, 0, 0.161)	(0, 0, 0.165)	(0, 0, 0.158)	(0, 0, 0.160)
Mn-O (1)	1.897 Å	1.932 Å	1.928 Å	1.915 Å
Mn-O (2)	2.018 Å	2.061 Å	1.997 Å	1.991 Å
Sr-O (1)	2.607 Å	2.618 Å	2.616 Å	2.625 Å
Sr-O (2)	2.693 Å	2.749 Å	2.734 Å	2.716 Å
Mn-O (1)/Mn-O (2)	0.94	0.94	0.96	0.96
R_p	7.7	7.18	6.18	7.18
R_{wp}	4.8	7.54	6.58	7.54
R_{exp}	6.9	4.94	4.69	4.94
χ^2	2.01	2.33	1.97	2.33
t	0.993	0.971	0.961	0.941
GII	0.33	0.32	0.30	0.30

4.3.2 Microstructural characterization

The effect of La substitution on morphology is studied using a scanning electron microscopy (SEM) technique. The recorded SEM images of the fractured surfaces of the sintered pellets are shown in Fig. 4.2 (a). The micrographs corresponding to each composition are homogeneous, showing well-developed grains, separated by well-defined grain boundaries, a typical characteristic feature of a polycrystalline material. A system change in the morphology is observed with increasing La substitution. For lower composition, i.e., x= 0.3, the grains are well separated, with increasing composition it starts agglomerating, forms clusters of grains. A histogram of the distribution of grain size for all the samples was obtained using the ImageJ software package. By fitting the Gaussian function to these histograms (Fig. 4.2 (b)) average grain size for all the samples was calculated and written on their respective histogram.

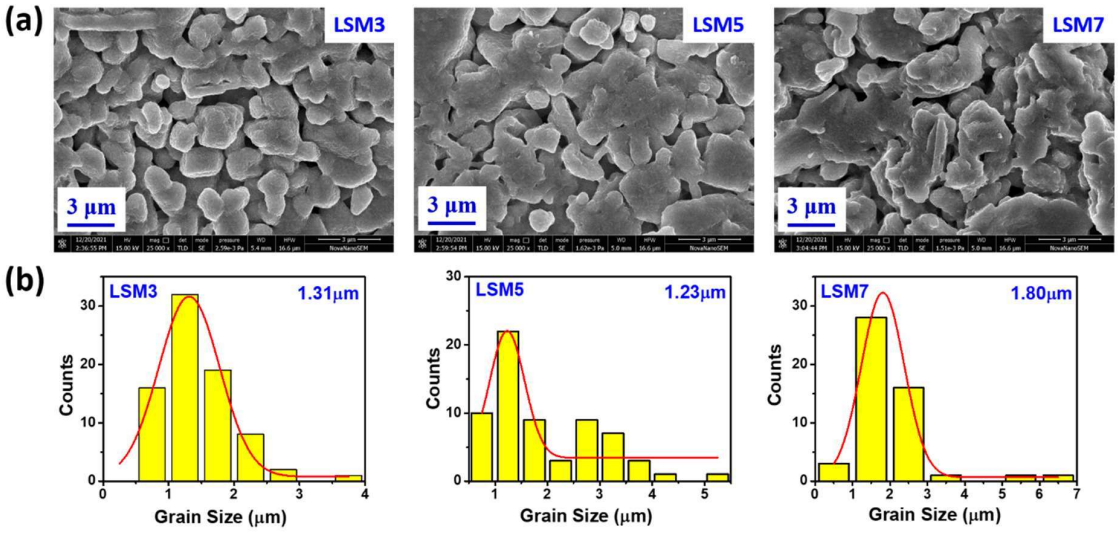

Figure 4.2. (a) SEM images of the fractured surfaces of the sintered pellets (b) Histograms showing the distribution of grain size in the samples.

4.3.3 X-Ray Photoelectron Spectroscopy Analysis

X-ray photoelectron spectroscopy (XPS) has been used to elucidate the valence state of the constituent ions Mn. Fig. 4.3 shows the core level Mn 2p spectra of the samples LSM5, and LSM7. All binding energies were calibrated based on the C 1s peak at 285 eV. The spectrum of Mn exhibits two primary peaks for all the samples corresponding to Mn $2p_{1/2}$ and $2p_{3/2}$ due to spin-orbit coupling [238,247]. The position of these peaks remains nearly same for all the samples. However, the broadening and asymmetry of the peaks are different for different samples. The peak corresponding to Mn $2p_{3/2}$ was deconvoluted to investigate the possible valence states. The XPS core level binding energy corresponding to different elements and their valence states are summarized in Table 4.2. Percentage (%) fractions of Mn^{3+} and Mn^{4+} are calculated from the peak area, also given in Table 4.2. It is already mentioned that these samples were prepared at 1500 ^oC, therefore loss of oxygen from the lattice is expected. According to defect chemistry, the loss of oxygen in Kröger–Vink notation is as follows:

$$O_o^{\times} \rightarrow V_o^{\bullet\bullet} + 2e' + \frac{1}{2}O_2(g) \uparrow \qquad (4.6)$$

The electrons released in Eqn. (4.6) may be captured by Mn^{4+} cations and reduced to Mn^{3+}. In the literature, it has been mentioned that the Sr_2MnO_4 phase can be stabilized at lower temperatures only when it contains around 30% Mn ions in Mn^{3+} state [73,241]. Reduction of Mn^{4+} state into Mn^{3+} state has been realized by synthesizing in a reducing atmosphere and quenching [238]. The donor doping of La in Sr_2MnO_4 at the Sr site has further reduced Mn^{4+} cation into the Mn^{3+} oxidation state, leading to an overall ~68% and ~79% concentration of Mn^{3+} in LSM5 and LSM7, respectively.

Table 4.2. XPS core level binding energy of Mn 2p and Nb 3d.

Elements	Mn $2p_{1/2}$	Mn $2p_{3/2}$		Concentration of Mn^{3+}
		Mn^{4+}	Mn^{3+}	
Sample Code	**B. E. (eV)**	**B. E. (eV)**	**B. E. (eV)**	**%**
LSM5	653.63	643.384	641.745	68.4
LSM7	653.79	643.907	642.002	79.1

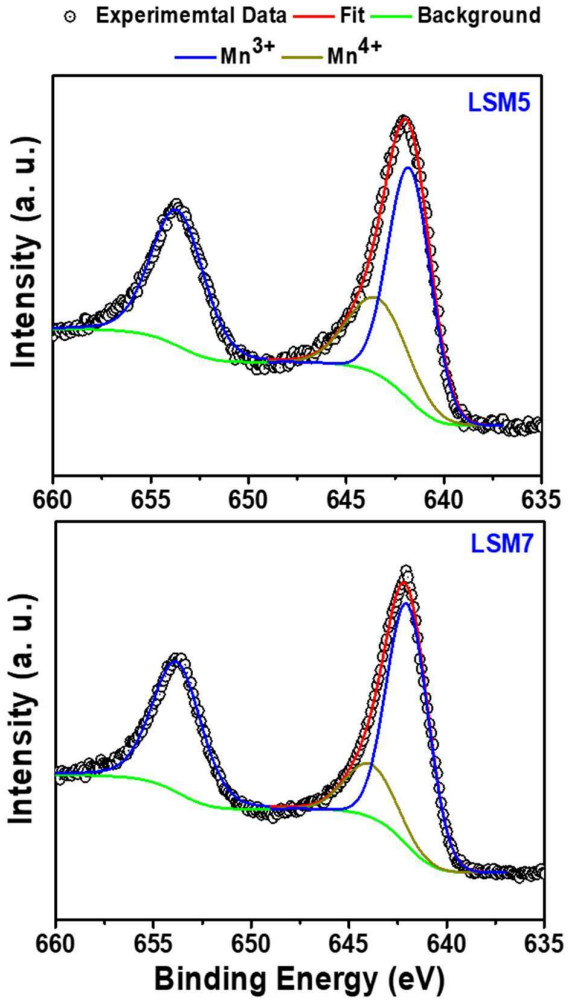

Figure 4.3. Core-level XPS spectra of Mn 2p.

4.3.4 Negative Permittivity Behaviour

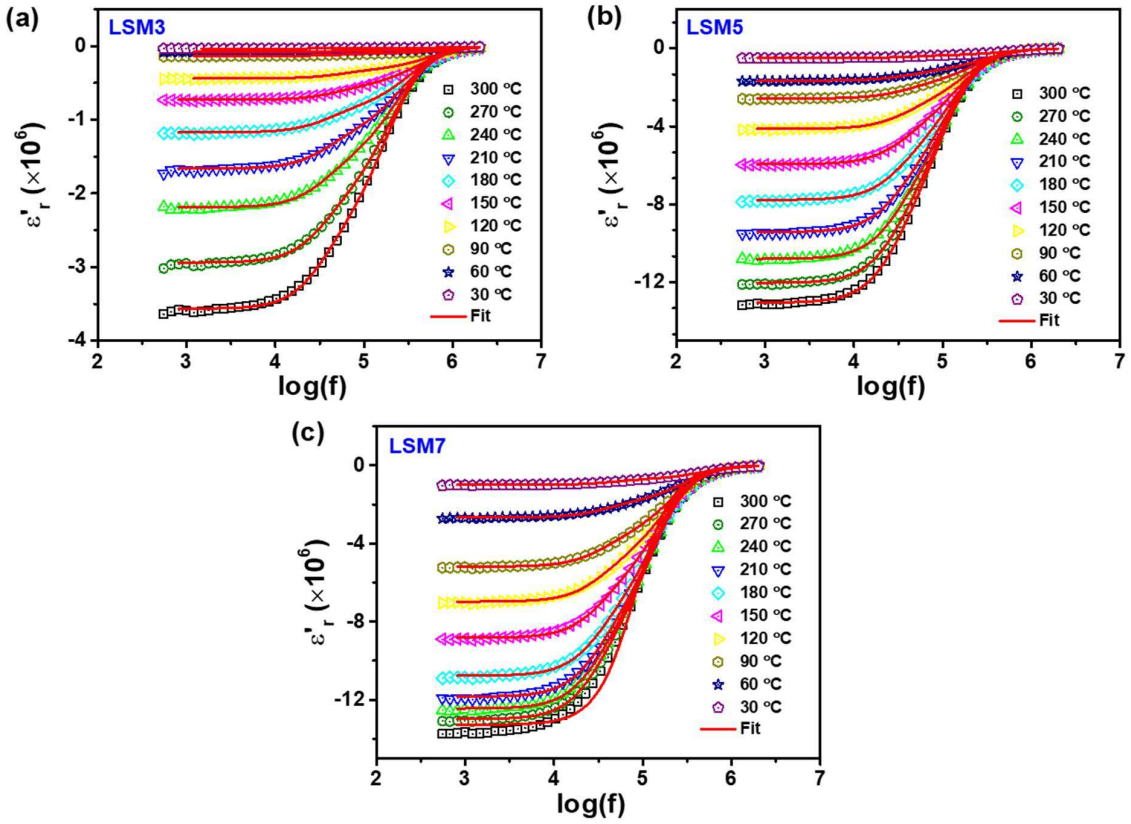

Figure 4.4.Variation of the real part of the relative permittivity with frequency at a few selected temperatures.

The permittivity of the samples was calculated from measured impedance data, by the following equation:

$$\varepsilon_r^* = \frac{1}{i\omega C_0 Z^*} \qquad (4.7)$$

where, $\varepsilon_r^* (= \varepsilon_r' - i\varepsilon_r'')$ is complex relative permittivity, i is an imaginary unit ($i^2 = -1$), ω is the angular frequency of the applied signal, $C_0 = \varepsilon_0 A/d$, ε_0 = permittivity of free space (8.85×10^{-12} Fm^{-1}), A = electrode surface area, d = separation between the electrodes and $Z^* (= Z' + iZ'')$ is the complex impedance. The variation of the real component of the relative permittivity, ε_r' with the frequency at few selected temperatures is shown in Fig. 4.4. In the frequency range 1 kHz to 2 MHz, values of ε_r' remain negative at all measuring temperatures

(30 °C -300 °C), but absolute values decrease with increasing frequency. In 1900 Drude proposed a model to explain the negative permittivity behaviour of metals [108,153,229,234]. We tried to fit the Drude model to the experimental data points shown in Fig. 4.4. It was observed that experimental data points are not in agreement with data generated according to the Drude model, the reason may be the presence of both bound (localized) and free (delocalized) electrons in the samples. The Drude-Lorentz (DL) model has been employed by the researchers to explain the negative permittivity behaviour of semiconductors possessing both localized (bound) and delocalized (free) charge carriers. According to this model, the real part of the complex permittivity (ε_r') is described as follows [236]:

$$\varepsilon_r' = \varepsilon_\infty - \frac{\omega_{pd}^2}{\omega^2 + \omega_d^2} + \frac{\omega_{pl}^2(\omega_0^2 - \omega^2)}{(\omega_0^2 - \omega^2)^2 + \omega^2\gamma^2} \qquad (4.8)$$

where, ε_∞ is the permittivity extrapolated towards high frequency, ω_{pl} is the Lorentz angular plasma frequency, ω_d is the damping frequency, ω_0 is the resonance frequency or damping force, γ damping coefficient of oscillating dipoles, ω_{pd} is the Drude angular plasma frequency, which is related to free charge carrier concentration (n_{free}), effective mass of free charge carriers (m_{free}^*) and, e is a charge of an electron (= 1.6×10^{-19} C)

$$\omega_{pd} = \sqrt{\frac{n_{free}.e^2}{m_{free}^*.\varepsilon_0}} \qquad (4.9)$$

similarly, the Lorentz angular plasma frequency, ω_{pl} is related to bound charge carrier concentration (n_{bou}), effective mass of oscillating dipoles (m_{bou}^*) and, charge of dipole (q).

$$\omega_{pl} = \sqrt{\frac{n_{bou}.q^2}{m_{bou}^*.\varepsilon_0}} \qquad (4.10)$$

By considering the presence of both free and bound charge carriers in the synthesized samples, the Drude-Lorentz (DL) model was fitted to the experimental data points as shown in Fig. 4.4. In Fig. 4.4 solid lines represent data generated according to the Drude-Lorentz model (Eqn. (4.8)) and symbols to the experimental data points. The ε_r' vs log f curves at different temperatures are in good agreement with the Drude-Lorentz model which confirms the presence of both free and bound charge carriers in both the samples up to the highest temperature of the measurement i.e., up to 300 ^oC. Absence of resonance characteristics in the experimental data can be due to dominating response of the plasmonic oscillations of free electrons over the resonance response of localized charges. A decreasing trend of the absolute value of negative permittivity with increasing frequency is accordance with the Drude model. The fitting parameters ω_{pd}, ω_{pl} ω_d, and γ, calculated while fitting Eqn. (4.8) to measured experimental data for different samples are plotted against temperature in Fig. 4.5. For comparing the values of these fitting parameters for different samples these values were divided by cell parameters k ($= A/d$; A = electrode surface area, d = separation between the electrodes). The Drude angular plasma frequency, ω_{pd} decreases with temperature, however, the Lorentz angular plasma frequency, ω_{pl} increases with temperature. The ω_{pd} varies with temperature due to volumetric effect as: $\omega_{pd}(T) = \omega_{pd_0}[1 + \beta(T - T_0)]^{-1/2}$, where, ω_{pd_0} is Drude angular plasma frequency at room temperature (T_0) and, β is the volume thermal expansion coefficient of ceramic [248]. The variation of ω_{pd} is consistent with this equation. The increase in ω_{pl} with temperature can be understood as: the number of bound charges, n_{bou} associated with oscillating dipoles, i.e., those present at the top of the valence band increases with temperature, due to thermal excitations of core electrons to the edge of the valence band, results in increasing ω_{pl} with temperature. The Drude angular plasma frequency, ω_{pd}; and Lorentz angular plasma frequency, ω_{pl} are also functions of free charge carriers' concentration, n_{free}

and bound charge carrier concentration, n_{bou}, respectively. Theoretically, La doping in Sr_2MnO_4 unit cells acts as donor doping, henceforth the increasing doping concentration of La will increase the effective charge carriers' concentration. The calculated values of ω_{pd} and ω_{pl} are in the order of LSM7 > LSM5 > LSM3, which is a signature of the donor nature of La in Sr_2MnO_4. The values of ω_d, and γ has also decreased with increasing temperature, which represents the weakening of binding forces associated with free and bound charges, respectively, with increasing temperature.

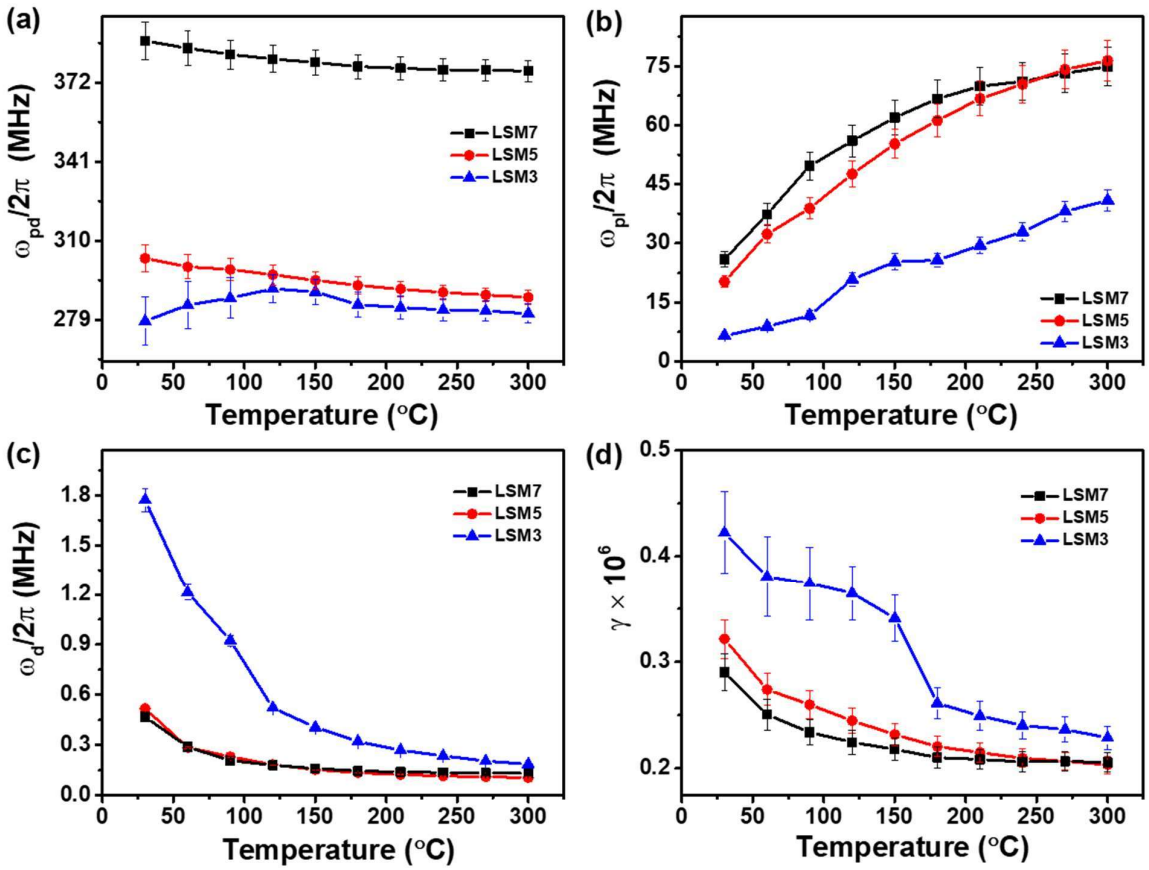

Figure 4.5. Variation of fitting parameters ($\omega_{pd}, \omega_{pl}, \omega_d, \gamma$) with temperature.

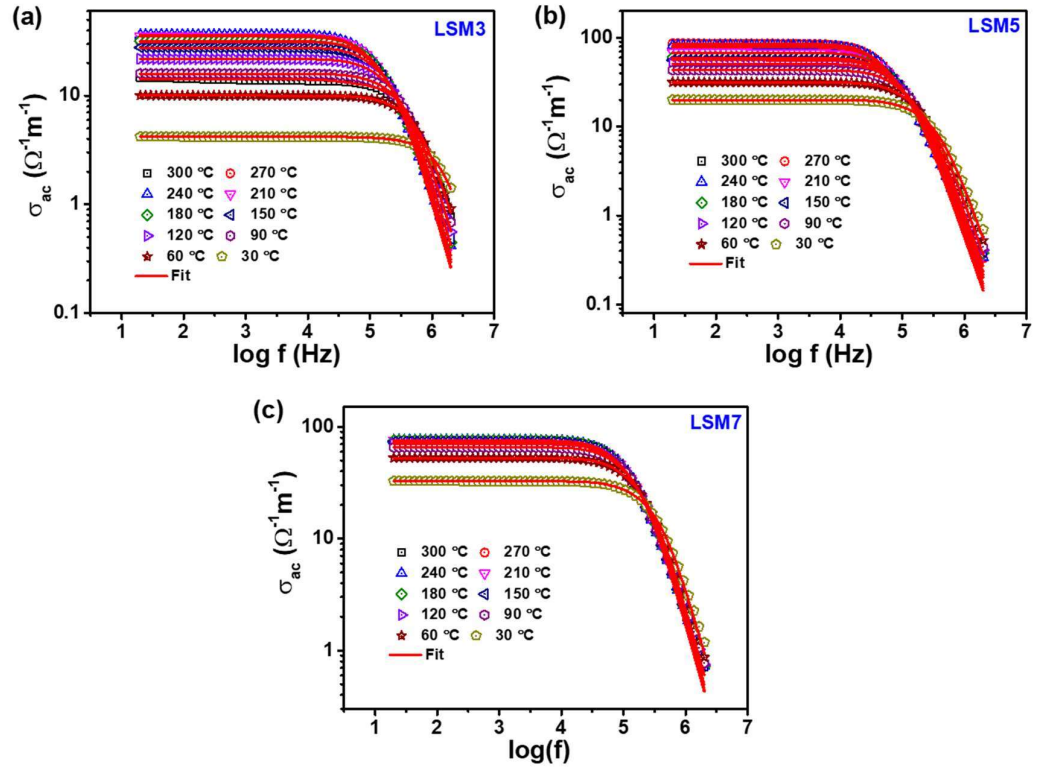

Figure 4.6. AC conductivity spectra of the samples at some representative temperatures.

The observed negative permittivity can be correlated with ac conductivity (σ_{ac}). Fig. 4.6 shows the frequency dependences of ac conductivity at few selected temperatures for all the samples. It's observed that the ac conductivity (σ_{ac}) remains constant up to a certain frequency and above that it decreases with the frequency (Fig. 4.6). The decreasing part of the conductivity showed the metal-like conduction behaviour (skin effect of the conduction electrons) in the samples. The Drude-Lorentz oscillator model was used to analyses ac conduction behaviour of the samples. According to this model, conductivity is related to various parameters as in the Eqn. (4.11) [236]:

$$\sigma_{ac} = \frac{\sigma_{dc}}{1+\omega^2\tau^2} + \frac{\varepsilon_0\omega_{pl}^2\omega^2\gamma}{(\omega_0^2-\omega^2)^2+\omega^2\gamma^2} \qquad (4.11)$$

where, σ_{dc} is the dc limit of Drude conductivity, τ is the average scattering time of carriers, ω_{pl} is the Lorentz angular plasma frequency, ω_0 is the resonance frequency, and γ is the damping factor. The first part of Eqn. (4.11) represents the contribution of free electrons,

while the second part to the resonance response of localized/bound electrons. In Fig. 4.6, symbols are experimentally measured data points and solid lines represent fitting according DL models. A good matching between measured data and data calculated according to Eqn. (4.11) is an evidence of dominating role of the free charge carriers over bound charge carriers.

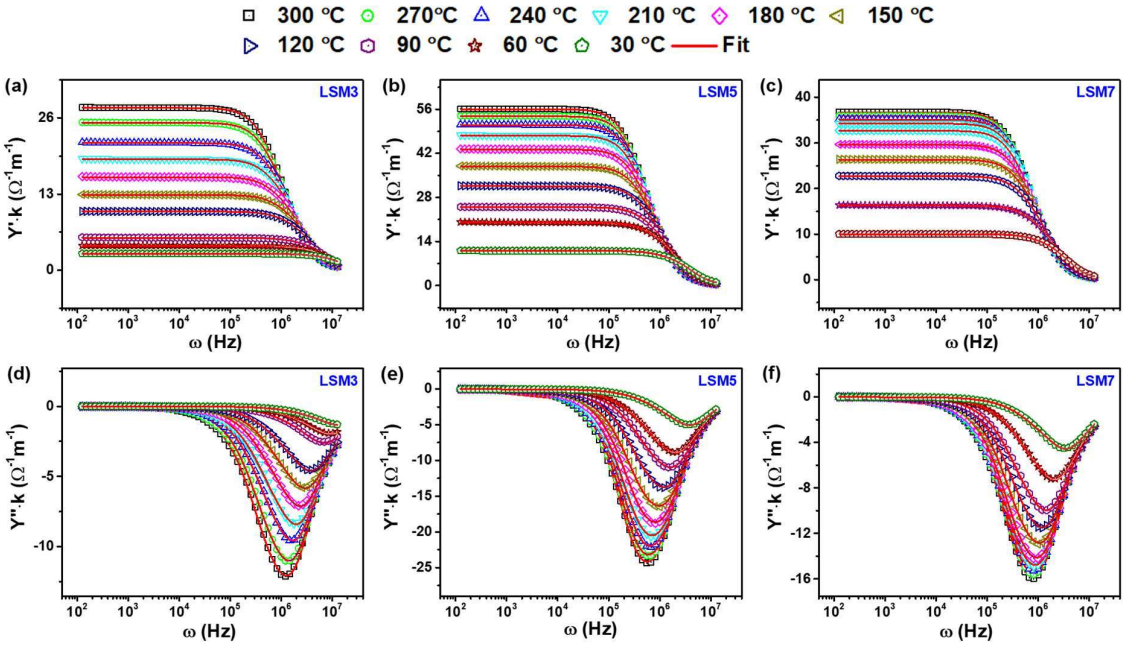

Figure 4.7. Variation of admittance with angular frequency at few selected temperatures.

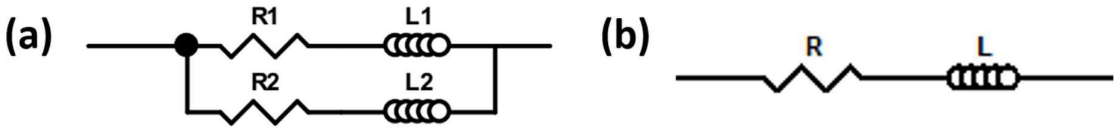

Figure 4.8. Optimum equivalent circuit.

To get insight into the origin of negative dielectric constant, the variation of impedance ($Z^* = Z' + iZ''$) with frequency at few selected temperatures are analysed. Generally, the frequency-dependent reactance is used to reveal the intrinsic electrical responses of materials in applied time varying electric field. The reactance is commonly expressed as $Z'' = Z_C + Z_L$, where Z_C is the capacitive reactance ($Z_C = -\frac{1}{\omega C}$, C is the capacitance) and Z_L is the inductive reactance ($Z_L = \omega L$, L is the inductance). In all samples positive reactance is observed in the

tested frequency range, suggesting that prepared ceramics present an inductive characteristic. The experimentally measured impedance (Z^*) has also a positive real part (Z'), which implies resistive characteristic of prepared samples. The measured impedance values are very small for all samples. Therefore, instead of impedance its inverse, i.e., admittance is used in study. The impedance and admittance are corelated with following Eqn.

$$Y^* = \frac{1}{Z^*} \tag{4.12}$$

$$Y' + iY'' = \frac{Z'}{|Z^*|^2} - i\frac{Z''}{|Z^*|^2} \tag{4.13}$$

i.e., the numerical values of imaginary part of admittance (Y'') will be negative when reactance (Z'') is positive. The variation of real and imaginary parts of admittance is shown in Fig.4.7. Here, it's important to note that the impedance provided by the sample holder and its connecting wires has unwittingly contributed to the experientially observed impedance values. Since the total measured impedance values are small in magnitude. Therefore, it's advisable and necessary to remove this unintentional contribution caused by the sample holder's impedance from experimentally collected data before analysing the reactance behaviour of synthesised samples. For this purpose, different combinations of resistors and inductors are used to model the experimentally measured impedance or admittance. The resistors and inductors combination shown in Fig. 4.8 (a) is found to be optimum for modelling experimentally measured impedance. The combination has two resistors (R_1 & R_2) and two inductors (L_1 & L_2). The values of R_1, R_2, L_1, L_2 calculated from fitting of impedance of samples measured at different temperatures are shown in Fig. 4.9. For comparing the values of R_1, R_2, L_1, L_2 for different samples here also these values were divided by cell parameters k. The values of R_1 & L_1 is smaller than R_2 & L_2, respectively. These are also almost temperature independent. However, R_2 & L_2 are temperature dependent and decreases with temperature.

To quantify the contribution from sample holder. The impedance of blank sample holder/without placing pellet in sample holder is measured. This measured impedance (admittance) data is model in similar fashion as measured impedance values of samples was done. For blank sample holder the resistors and inductors combination shown in Fig. 4.8 (b) is found to be optimum. The calculated values of resistance (R) and inductance (L) of sample holder matches very well with the calculated values of R_1 & L_1 for sample. The R_1 & L_1 were also temperature independent while R_2 & L_2 are temperature dependent and decreases with temperature. The properties of sample holder should be temperature independent. Hence forth, I have attribute R_1, L_1 to sample holder contribution while R_2, L_2 to sample's resistance and inductance.

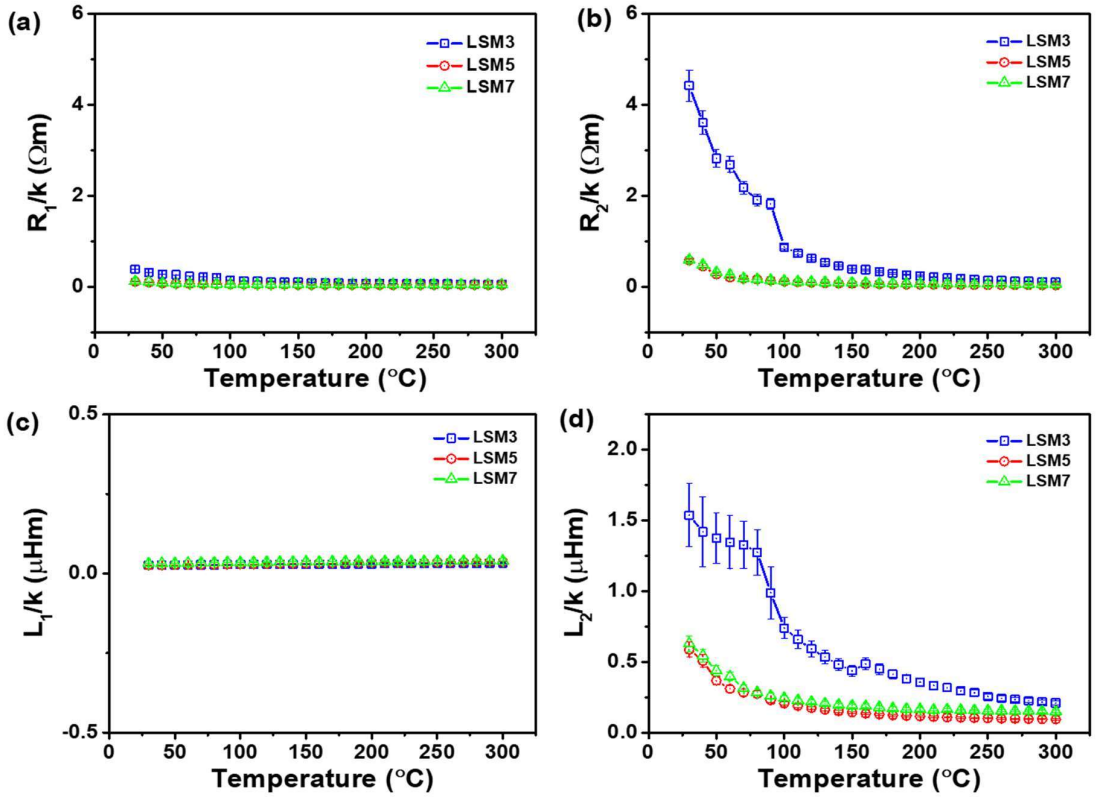

Figure 4.9. Variation in the values of equivalent circuit elements (R_1, R_2, L_1, L_2) with temperature.

The calculated relative permittivity had a good agreement with DL model (Fig. 4.4). And the study ac conductivity also shown a good resemblance with DL model. According DL

model the plasmonic oscillation of free charge carriers are responsible for negative dielectric behaviour. The plasmonic oscillation of these charge carriers in applied sinusoidal electric filed gives rise to surface current. The origination of inductance behaviour (L_2) of the sample can we attributed to these surface/plasmonic current on grains surface of the sample. And the resistance (R_2) can be attributed to resistance offered to this circulating current on grains' surface and/or resistance offered to conduction current within/through the grains. The increasing temperature of sample will affect the response of free charge carriers in the applied sinusoidal electric field and weakens it with increasing temperature due to increasing thermal agitation. Thereby the inductance, L_2 of sample decreases with increasing temperature (Fig. 4.9 (d)). However, due to semiconducting nature of sample the resistance, R_2 decreases with increasing temperature (Fig. 4.9 (b)).

4.4 Conclusions

The powder and ceramic of La substituted layered oxides $La_xSr_{2-x}Mn_{1-x}O_4$ (x = 0.3, 0.5, 0.7) were synthesized using the solid-state reaction technique. The Rietveld refinement confirmed tetragonal structure with space group I4/mmm same as of the Sr_2MnO_4 for all synthesized compositions (x = 0.3, 0.5, 0.7). SEM images have clearly exhibited changes in the grain's morphologies on La substitution. XPS analysis indicated the presence of Mn in mixed-valence states Mn^{3+}- Mn^{4+}. Studies of permittivity and AC conductivity with respect to temperature and frequency have shown negative permittivity in the entire range of the measurement (30 – 300 ^oC). The observed negative permittivity in the frequency range 1 kHz-2 MHz is attributed to plasmonic oscillations of free carriers, generated by the thermal excitation process. A good matching between experimental data (ε_r' and $\log \sigma_{ac}$ vs $\log f$ plots) and data generated according to the Drude-Lorentz model confirmed the presence of both localized and free charge carriers in the samples. The inductive character of the samples is shown by the modelling of

impedance data using various combinations of resistors and inductors. The inductive character of samples shows the prospect of developing synthesized compositions as coil-less inductor.